Journal of Solid State Chemistry 279 (2019) 120964

Contents lists available at ScienceDirect

Journal of Solid State Chemistry

Synthesis and optical properties RE_2O_2S:Ln (RE = La, Y; Ln = Ce, Eu, Dy, Er)

E.I. Sal'nikova [a,b,*], YuG. Denisenko [c], A.S. Aleksandrovsky [d,e], I.E. Kolesnikov [f,g], E. Lähderanta [g], P.O. Andreev [a], N.O. Azarapin [a], O.V. Andreev [a], S.A. Basova [a], A.V. Matigorov [a]

[a] Department of Inorganic and Physical Chemistry, Tyumen State University, Tyumen, 625003, Russia
[b] Department of General Chemistry, Northern Trans-Ural Agricultural University, Tyumen, 625003, Russia
[c] Department of General and Special Chemistry, Industrial University of Tyumen, Tyumen, 625000, Russia
[d] Laboratory of Coherent Optics, Kirensky Institute of Physics Federal Research Center KSC SB RAS, Krasnoyarsk, 660036, Russia
[e] Institute of Nanotechnology, Spectroscopy and Quantum Chemistry, Siberian Federal University, Krasnoyarsk, 660041, Russia
[f] Center for Optical and Laser Materials Research, St. Petersburg State University, St. Petersburg, 199034, Russia
[g] Department of Physics, Lappeenranta University of Technology LUT, Lappeenranta, 53850, Finland

ARTICLE INFO

Keywords:
Oxysulfides
Sulfates
Rare-earth
Reduction
Optical ceramic
Luminescence

ABSTRACT

The phase formation sequence was studied in the preparation of solid solutions of RE_2O_2S: Ln' (RE = La, Y; Ln' = Ce, Eu, Dy, Er) by the reduction of the match co-precipitated sulfates, followed by sulfidization of the reduction products. For uniform distribution of cations in the matrix, a method of chemical homogenization was used, consisting in the preparation of an aqueous solution containing all the necessary cations and their subsequent precipitation in the form of sulfates. The use of sulfates as precursors facilitates the process of obtaining solid solutions of oxysulfides, since sulfates already contain SO_4^{2-}-ions. The phase and morphological certification of the obtained solid solutions was carried out. The study of steady state luminescent properties demonstrated characteristic bands which are assigned to *4f-4f* and *5d-4f* transition. The obtained results showed the possibility of applying the method to synthesize optical ceramics based on solid solutionsRE_2O_2S: Ln (RE = La, Y; Ln = Ce, Eu, Dy, Er).

1. Introduction

Oxygen-containing compounds of rare-earth elements have long attracted the attention of researchers due to their effective luminescent properties, which have found application in many optical systems [1–6]. Despite the fact that the luminescence is mainly determined by the nature of the substituting ion, the host matrix into which this ion is embedded influences on the emission lines intensity through its crystal field [7–10]. Lanthanide ions can emit light in the near UV, visible and infrared regions of the spectrum. Each ion has a characteristic absorption and emission spectrum. Ln^{3+} radiations characterized by high color purity; therefore, materials activated by lanthanides are attractive for creating LEDs, fluorescent lamps, plasma displays, and active media for solid-state lasers [11–13].

Activated materials based on oxisulfides of rare-earth elements are widely used in various fields [14–22]. However, in recent years, only laborious, poorly reproducible methods of producing nanoparticles are described in the literature for these objects. At the same time, the need for relatively simple synthesis methods allowing large batches of optical ceramics does not decrease [23–27].

Thermal decomposition methods are convenient for obtaining materials with different properties [28–32]. In the preparation of oxysulfides, particular attention is drawn to methods for reducing sulfur containing compounds to higher oxidation degrees. Compared with solid-phase methods, the recovery method differs in manufacturability, reproducibility, and the ability to produce several tens of grams of a product at once [33–39].

Thus, the aim of the work is to study the chemistry of reactions in the sequential processing of co-precipitated sulfates of rare earth elements in the atmosphere of H_2, H_2S to obtain activated oxysulfides and investigate the morphology of the obtained reaction products and their luminescent properties.

2. Materials and methods

2.1. Preparative methods

Powders of co-precipitated sulfates were obtained by precipitation from a nitrate solution with concentrated sulfuric acid. For the

* Corresponding author.Tyumen State University, Tyumen, 625003, Russia.
E-mail address: elenasalnikova213@gmail.com (E.I. Sal'nikova).

https://doi.org/10.1016/j.jssc.2019.120964
Received 2 July 2019; Received in revised form 17 August 2019; Accepted 17 September 2019
Available online 18 September 2019

synthesis, high purity reagents were used: Ln_2O_3 (≥ 99.99%, ultrapure, TDM-96 Ltd. Russia). Concentrated nitric acid solution ($C(HNO_3) = 14.6$ mol/L, ultrapure, Vekton Ltd., Russia), concentrated sulfuric acid solution ($C(H_2SO_4) = 17.9$ mol/L, ultrapure, Vekton Ltd., Russia). Weighing was carried out on an analytical balance with an accuracy of 0.1 mg. Before weighing, the oxides were calcined in a muffle furnace at a temperature of 1000 °C for 12 h to remove sorbed gases and products of their interaction with oxides ($Ln(OH)_3$, $Ln_2(CO_3)_2$). Acid solutions were measured using glass measuring cylinders with an accuracy of 0.1 ml.

The calculated weighed amount of oxides with a total weight of 5.0 g was placed in a 100 mL glass round-bottom flask, then 7.0 mL of a concentrated solution of nitric acid was poured in small portions. The reaction mixture was heated on a mantle until the oxides were completely dissolved. As a result, a nitrate solution was obtained with evenly distributed cations:

$$0.99RE_2O_3 + 0.01Ln_2O_3 + 6HNO_3 \rightarrow 2(RE_{0.99}Ln_{0.01})(NO_3)_3 + 3H_2O \quad (1)$$

After cooling the solution, 3.0 mL of concentrated sulfuric acid was poured in small portions to it, avoiding strong heating of the reaction mixture. As a result, a precipitate of co-precipitated sulfates and their crystalline hydrates forms:

$$2(RE_{0.99}Ln_{0.01})(NO_3)_3 + 3H_2SO_4 + nH_2O \rightarrow (RE_{0.99}Ln_{0.1})_2(SO_4)_3{\cdot}nH_2O + 6HNO_3 \quad (2)$$

After carrying out the precipitation reaction, the reaction mixture is distilled off to the dry residue. The obtained polycrystalline product is additionally calcined in a tubular furnace at a temperature of 500 °C to remove sorbed moisture and acids. Later, the powder is annealed at the same temperature for 7 days, in order to form an acceptable crystallite structure.

This method of chemical homogenization has a number of significant advantages:

- In the process of synthesis, no cations other than Ln^{3+} are added to the reaction mixture, which excludes their replacement and the formation of defects in the crystal structure.
- Sulfates precipitate from a homogeneous nitrate solution, which ensures high stoichiometry and uniform distribution of cations within the crystal lattice.
- Conducting the reaction in an environment of concentrated sulfuric acid allows to form the structure of anhydrous sulfate at the earliest stages.

The reduction of sulfates in a hydrogen atmosphere was carried out on the apparatus shown in Fig. S1. High purity hydrogen was obtained by the electrolytic method in the SPECTR - 6 M hydrogen generator. The temperature in the furnace was set using a microprocessor controller. The temperature in the furnace was controlled using chromel-alumel thermocouple. A weighed amount of co-precipitated sulfates was placed in a quartz reactor, and for 30 min it was purged with hydrogen from a generator at a rate of 6 L/h. After that, the reactor was placed in a heated vertical furnace and kept for the required amount of time. After completion of the process, the rector was removed from the furnace and cooled to room temperature.

Processing of the reduced products in an atmosphere of hydrogen sulfide was carried out on a similar setup (Fig. S2). The difference lies in the fact that before being fed into the reactor, the hydrogen passes through a flask with molten elemental sulfur and heated to 350 °C. As a result, hydrogen sulfide is formed:

$$H_2 + S \rightarrow H_2S \quad (3)$$

Consequently, it is not a hydrogen inflows the reactor, but a hydrogen sulfide.

2.2. Methods of physical-chemical analysis

X-ray phase analysis (XRD) was performed on a BRUKER D2 PHASER diffractometer with a linear detector LYNXEYE (CuKα radiation, Ni-filter). Rietveld refinement of all six samples was performed by using TOPAS 4.2 [40]. Almost all peaks were indexed.

Electron-microscopic analysis was carried out on electron microscope JEOL JSM-6510LV. X-ray energy-dispersive analyzer was used to register X-rays at element spectrum plotting in selected sample surface areas. The inaccuracy in element content determination was equal to ±0.2%.

All measurements of the luminescent properties were carried out on a research-grade spectrofluorimeter. Horiba JobinYvon Fluorolog-3 equipped with double monochromators for excitation and emission channels and 450 W xenon lamp as an excitation source.

3. Result and discussion

3.1. Synthetic experiment

Detailed consideration of the chemical transformations taking place during the transformation of co-precipitated sulfates into the corresponding solid solutions of oxysulfides was made on the basis of two model systems $La_2(SO_4)_3$:Dy^{3+} and $Y_2(SO_4)_3$:Er^{3+}. The results obtained were used to synthesize all other solid solutions, which are reported in this work.

The carrying out of the co-precipitation of sulfates and the subsequent annealing led to the formation of structures of solid solutions of sulfates in which the doping ion is fully incorporated into the crystal lattice of the matrix and occupies the crystallographic positions of the host cation. According to X-ray diffraction data, all samples of co-precipitated sulfates are single-phase (Fig. 1a and b). There is a slight shift in the unit cell parameters caused by the difference in the radii of the cations of the matrix and the dopant.

The appearance of gaseous reduction products was recorded at a temperature of 570 °C. In this connection, sulfate reduction was carried out at t = 600 °C. At this temperature, after 60 min of the process, the products mainly consist of 4 phases: $(RE_{0.99}Ln_{0.01})_2(SO_4)_3$-$(RE_{0.99}Ln_{0.01})_2O_2SO_4$ - $(RE_{0.99}Ln_{0.01})_2O_2S$ - $(RE_{0.99}Ln_{0.01})_2O_3$ (Fig. 1c and d). There was an incomplete transformation of the initial sulfates into the reaction products. The following chemical equations correspond to the formation of the corresponding reduction products:

$$(RE_{0.99}Ln_{0.01})_2(SO_4)_3 + 6H_2 \rightarrow (RE_{0.99}Ln_{0.01})_2O_2SO_4 + 2S + 6H_2O \quad (4)$$

$$(RE_{0.99}Ln_{0.01})_2(SO_4)_3 + 10H_2 \rightarrow (RE_{0.99}Ln_{0.01})_2O_2S + 2S + 10H_2O \quad (5)$$

$$(RE_{0.99}Ln_{0.01})_2(SO_4)_3 + 5H_2 \rightarrow (RE_{0.99}Ln_{0.01})_2O_3 + 2SO_2 + 5H_2O \quad (6)$$

$$(RE_{0.99}Ln_{0.01})_2O_2SO_4 + 4H_2 \rightarrow (RE_{0.99}Ln_{0.01})_2O_2S + 4H_2O \quad (7)$$

After 10 h of carrying out the process at a given temperature, polycrystalline products consist of two phases: $(RE_{0.99}Ln_{0.01})_2O_2S$, $(RE_{0.99}Ln_{0.01})_2O_3$ (Fig. 1e and f). The absence of compounds containing sulfur in the highest degree of oxidation of in the synthesis products indicates on a complete redox transformation. In all samples, the phase output $(RE_{0.99}Ln_{0.01})_2O_2S$ was not lower than 80%. Thus, the stage of sulfate reduction in a hydrogen atmosphere allows the formation of two-phase polycrystalline intermediates with a predominant content of the oxysulfide phase, which should greatly facilitate the sulfidation procedure.

The interaction of two-phase intermediates with hydrogen sulfide at a temperature of 800 °C for 5 h leads to the formation of single-phase powders $(RE_{0.99}Ln_{0.01})_2O_2S$ (Fig. 1g and h). The transformation corresponds to the transformation of the oxide phase to the oxysulfide under the action of a mild sulfiding agent H_2S:

$$(RE_{0.99}Ln_{0.01})_2O_3 + H_2S \rightarrow (RE_{0.99}Ln_{0.01})_2O_2S + H_2O \quad (8)$$

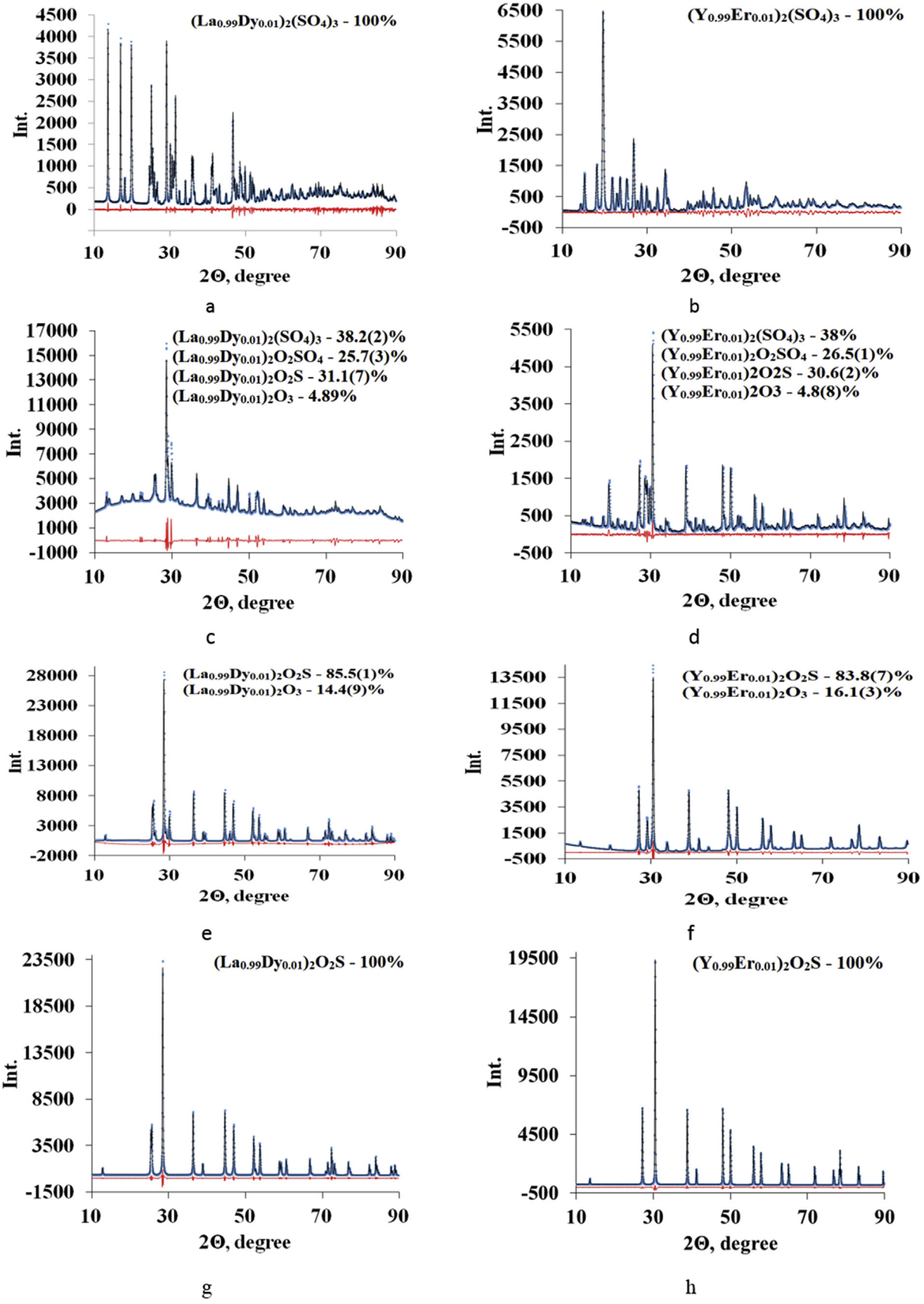

Fig. 1. Experimental, calculated, and difference Rietveld plot of: (a,b) $(RE_{0.99}Ln_{0.01})_2(SO_4)_3$; (c,d) $(RE_{0.99}Ln_{0.01})_2(SO_4)_3$-$(RE_{0.99}Ln_{0.01})_2O_2SO_4$-$(RE_{0.99}Ln_{0.01})_2O_2S$-$(RE_{0.99}Ln_{0.01})_2O_3$; e,f) $(RE_{0.99}Ln_{0.01})_2O_2S$ - $(RE_{0.99}Ln_{0.01})_2O_3$; (g,h) $(RE_{0.99}Ln_{0.01})_2O_2S$.

Sulfate powders, formed predominantly by loose agglomerates (Fig. 2, a) with sizes up to 10 μm. The resulting oxysulfide powders have a more distinct cut shape, a denser structure and a uniform size distribution (Fig. 2, a). The morphological transformation is evidently due to the elevated temperatures and the diffusion character of the reduction and sulfidation processes.

The enlargement obviously occurs as a result of the desire of the system to lower its energy. What corresponds to a decrease in the surface area of the polycrystalline samples. Particle cutting appears as a result of high rates of chemical reactions and rapid mass transfer. The indicated tendency to particle aggregation is often observed during similar processes [27,32–35].

3.2. Structural and spectroscopic properties

Crystal structure of both hosts belongs to *P-3m 1* space group of trigonal symmetry class. Y and La occupy a single inequivalent site. In both oxysulfides the local environment of them is a distorted polyhedron with seven vertices, four of them being oxygen ions and three being sulfur ions. Layered structure of oxysulfides implies that sulfur and oxygen are positioned in opposite hemispheres of the local environment of either Y or La. Rare-earth doping ions are expected to occupy Y and La sites, and their local environment is determined by the structure host, with the local symmetry C_{3v}. Therefore, absence of inversion symmetry must be pronounced in optical spectra of doping ions. Variation of luminescence properties of doping RE ions in one host with respect to another is usually ascribed to the change of the extent of inversion symmetry violation. Examining the geometry of local environment of RE ion in Y_2O_2S and La_2O_2S (Fig. 3) we observe that both environments are geometrically identical.

The excitation and emission spectra of RE_2O_2S (RE = Y, La) activated by 1% of Dy^{3+} ions are shown in Fig. 4. The observed spectra exhibit characteristic intra-configurational 4f-4f transitions. Excitation spectrum of $Y_2O_2S:Dy^{3+}$ monitored at 579 nm ($^4F_{9/2}$–$^6H_{13/2}$), displays following transitions: $^6H_{15/2}$–$^4P_{7/2}$ (355 nm), $^6H_{15/2}$–$^4P_{5/2}$ (369 nm), $^6H_{15/2}$–$^4I_{13/2}$ (388 nm), $^6H_{15/2}$–$^4G_{11/2}$ (427 nm), $^6H_{15/2}$–$^4I_{15/2}$ (451 nm) and $^6H_{15/2}$–$^4F_{9/2}$ (479 nm). The emission spectrum $Y_2O_2S:Dy^{3+}$ sample is dominated by green-yellow band (579 nm) corresponding to the hypersensitive $^4F_{9/2}$–$^6H_{13/2}$ transition. Other observed lines are attributed to the $^4I_{15/2}$–$^6H_{15/2}$ (457 nm), $^4F_{9/2}$–$^6H_{15/2}$ (487 nm), and $^4F_{9/2}$–$^6H_{11/2}$ (670 nm) transitions. It is well-known that $^4F_{9/2}$–$^6H_{13/2}$ is the forced electric dipole transition, which is hypersensitive and its intensity can vary by orders of magnitude depending on the local site symmetry, whereas $^4F_{9/2}$–$^6H_{15/2}$ transition intensity is insignificantly affected by the environment [40–42]. The excitation and emission spectra of $La_2O_2S:Dy^{3+}$ are similar to the $Y_2O_2S:Dy^{3+}$ ones. Small blue shift of bands and redistribution between them were observed. So, the most prominent transitions in excitation and emission spectra of $La_2O_2S:Dy^{3+}$ are centered at 353 and 576 nm, respectively. Observed luminescence spectra of Dy ion are consistent with the concept that they occupy Y(La) sites with the local symmetry C_{3v}.

To compare the crystal structure and crystal field of $Y_2O_2S:Dy^{3+}$ and $La_2O_2S:Dy^{3+}$ powders, we calculated ratio (R_{Dy}) between $^4F_{9/2}$–$^6H_{13/2}$ and $^4F_{9/2}$–$^6H_{15/2}$ intensities. This parameter is similar to the well-known asymmetry ratio for Eu^{3+} ions [43,44]. R_{Dy} value give information about the local surrounding and environmental changes near the Dy^{3+} ions. The higher the calculated parameter is, the more apart from a centrosymmetric geometry luminescent center is located. It is well-known that if Dy^{3+} is located at low symmetry without the inversion symmetry, the yellow emission is the most intense of all the transitions, as is the case with our synthesized nanocrystalline phosphors [45]. Experimental R_{Dy} values for $Y_2O_2S:Dy^{3+}$ and $La_2O_2S:Dy^{3+}$ samples are 3.13 and 4.65. In view of geometrical identity of local environments, this difference must be ascribed to the interplay between ionic radii of Y and La and the unit cell parameters, i.e. closer ligands at the same degree of inversion symmetry violation.

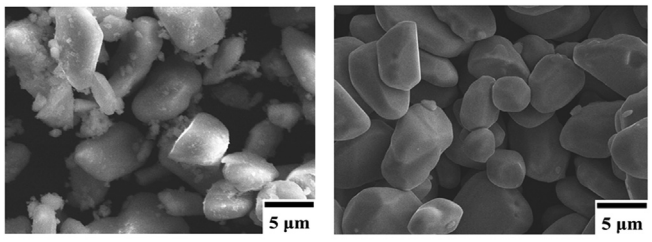

Fig. 2. SEM image of; (a) $(La_{0.99}Dy_{0.01})_2(SO_4)_3$; (b) $(La_{0.99}Dy_{0.01})_2O_2S$.

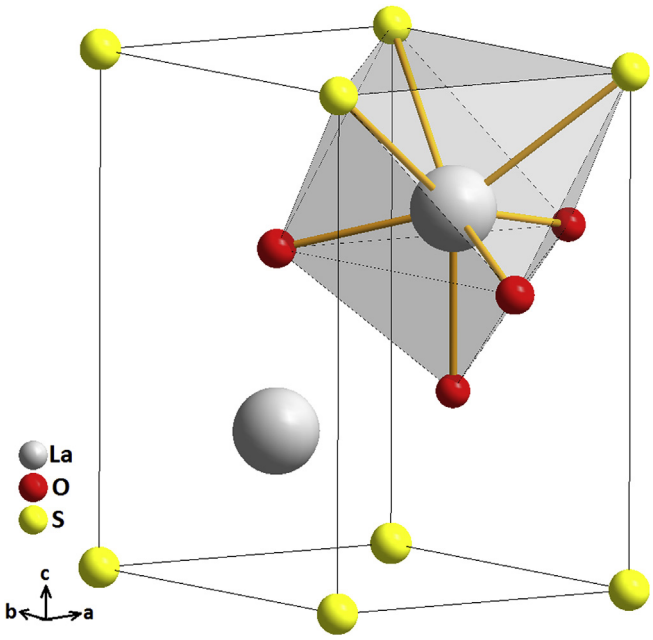

Fig. 3. Coordination polyhedron structure La_2O_2S.

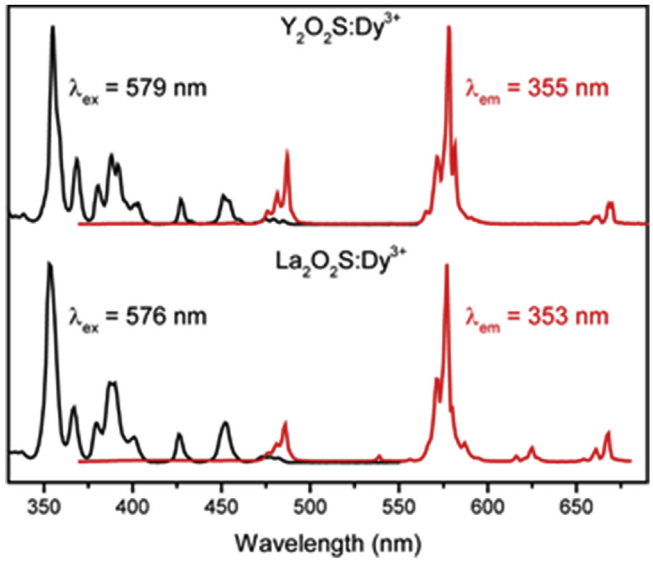

Fig. 4. Excitation and emission spectra of $Y_2O_2S:Dy^{3+}$ and $La_2O_2S:Dy^{3+}$ phosphors.

The steady state luminescence spectra of RE_2O_2S (RE = Y, La) powders doped with 1% of Er^{3+} ions are presented in Fig. 5. The excitation spectrum of $Y_2O_2S:Er^{3+}$ was monitored at 549 nm ($^4F_{9/2}$–$^4I_{15/2}$) within

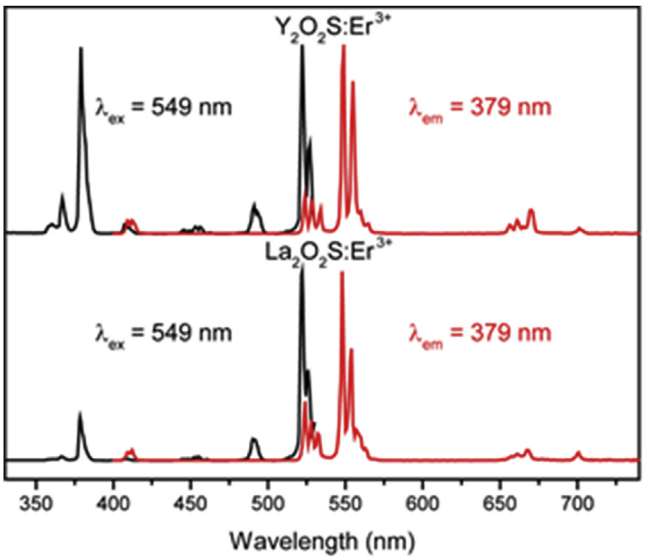

Fig. 5. Excitation and emission spectra of $Y_2O_2S:Er^{3+}$ and $La_2O_2S:Er^{3+}$phosphors.

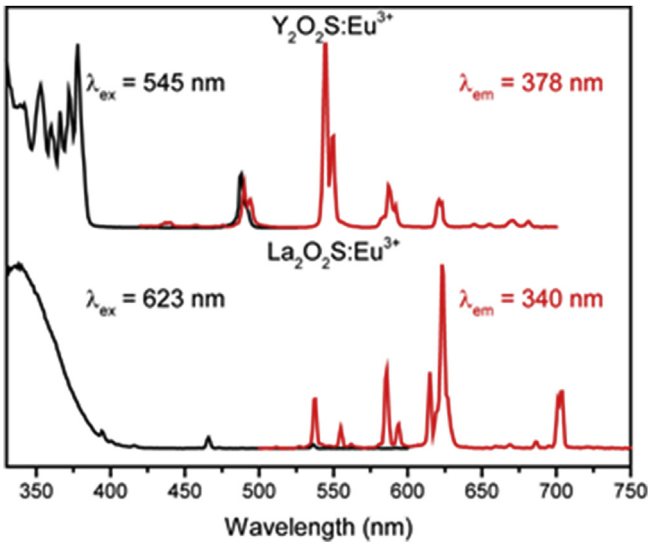

Fig. 6. Excitation and emission spectra of $Y_2O_2S:Eu^{3+}$ and $La_2O_2S:Eu^{3+}$phosphors.

spectral range of 330–530 nm. It consists of $^4I_{15/2}$–$^4G_{7/2}$ (360 nm), $^4I_{15/2}$–$^4G_{9/2}$ (367 nm), $^4I_{15/2}$–$^4G_{11/2}$ (379 nm), $^4I_{15/2}$–$^2H_{9/2}$ (408 nm), $^4I_{15/2}$–$^4F_{3/2}$ (446 nm),$^4I_{15/2}$–$^4F_{5/2}$ (453 nm),$^4I_{15/2}$–$^4F_{7/2}$ (491 nm), and $^4I_{15/2}$–$^2H_{11/2}$ (522 nm). The emission spectrum includes narrow bands, which are assigned to the following transitions: $^2H_{9/2}$–$^4I_{15/2}$ (409 nm), $^2H_{11/2}$–$^4I_{15/2}$ (524 nm), $^4S_{3/2}$–$^4I_{15/2}$ (549 nm), and $^4F_{9/2}$–$^4I_{15/2}$ (670 nm). The spectral line positions of $La_2O_2S:Er^{3+}$ spectra are the same. Change of host leads to the intensity redistribution, which is most pronounced for $^4I_{15/2}$–$^4G_{11/2}$ transition in the excitation spectrum.

Fig. 6 displays excitation and emission spectra of RE_2O_2S (RE = Y, La) activated by 1% of Eu^{3+} ions. The excitation spectrum of $Y_2O_2S:Eu^{3+}$ monitored at 545 nm ($^5D_1$–$^7F_1$) consists of following transitions:$^7F_0$–$^5D_4$ (353 nm),$^7F_0$–$^5L_7$ (378 nm) and $^7F_2$–$^5D_2$ (488 nm). The emission spectrum shows narrow bands originating from $^5D_1$and $^5D_0$ excited levels. Surprisingly, that the emission spectrum of $Y_2O_2S:Eu^{3+}$ is dominated by transition$^5D_1$–$^7F_1$ (545 nm), whereas the most prominent luminescence bands are usually attributed to the $^5D_0$–^7F_J transition [46–48]. Such behavior was previously reported for $La_2O_2S:Eu^{3+}$ bulk phosphors [49,50].

Dominance of $^5D_1$ emission can be explained by small phonon energy in regarded host, because significant amount of ions relax to $^5D_1$ level after the UV excitation, and they radiatively decay to the ground state before nonradiative decay to $^5D_0$ metastable level. We also observed $^5D_2$–$^7F_2$ (490 nm), $^5D_1$–$^7F_3$ (587 nm), $^5D_0$–$^7F_1$ (592 nm), $^5D_0$–$^7F_2$ (621 nm) and $^5D_0$–$^7F_3$ (670 nm) transitions.

The excitation and emission spectra of $La_2O_2S:Eu^{3+}$ display situation, which is more usual for Eu^{3+}-doped compounds. The excitation spectrum of $Y_2O_2S:Eu^{3+}$ monitored at 623 nm ($^5D_0$–$^7F_2$) consists of broad intense band corresponding to charge transfer S^{2-}–Eu^{3+} (338 nm) and low-intense line assigned to the typical intra-configurational transitions of the Eu^{3+} ion: $^7F_0$–$^5L_6$ (394 nm), $^7F_0$–$^5D_2$ (466 nm), $^7F_0$–$^5D_1$ (536 nm) and $^7F_1$–$^5D_0$ (593 nm). The emission spectrum is dominated by the forced electric dipole transition $^5D_0$–$^7F_2$ with maximum at 623 nm. Other observed lines are attributed to the $^5D_1$–$^7F_1$ (538 nm), $^5D_1$–$^7F_2$ (555 nm), $^5D_1$–$^7F_3$ (586 nm), $^5D_0$–$^7F_1$ (594 nm), $^5D_0$–$^7F_3$ (670 nm) and $^5D_0$–$^7F_4$ (704 nm).

Due to the unique luminescence properties of Eu^{3+} ions, it is quite easy to analyze the luminescent center local surrounding and its symmetry using only emission spectrum. The asymmetry ratio (R_{Eu}) gives information about local changes around the Eu^{3+} ions. It is defined as intensity ratio of forced electric dipole $^5D_0$–$^7F_2$ and magnetic dipole $^5D_0$–$^7F_1$ transitions. The higher the asymmetry parameter R_{Eu} is, the more apart from a centrosymmetric geometry luminescent center is located. The calculated R_{Eu} values of $Y_2O_2S:Eu^{3+}$ and $La_2O_2S:Eu^{3+}$ samples are 0.58 and 3.16, respectively. It is worth noting that the calculated R_{Eu} values of $Y_2O_2S:Eu^{3+}$ and $La_2O_2S:Eu^{3+}$ samples significantly differ, which indicate big difference in local surrounding of Eu^{3+} ions in these hosts.

The steady state luminescence spectra of RE_2O_2S (RE = Y, La) powders doped with 1% of Ce^{3+} ions are shown in Fig. 7. The excitation spectrum of $Y_2O_2S:Ce^{3+}$ sample displays two broad bands centered at 265 and 407 nm (λ_{em} = 545 nm). These bands correspond to direct excitation of the Ce^{3+} ions via transitions to the components of Ce^{3+} 5d configuration. The emission spectrum also consists of two lines attributed to allowed 5d–4f transition of Ce^{3+} ion. Generally, emission lines attributed to allowed 5d–4f transition in Ce^{3+}-doped materials are quite broad [51,52]. Sometimes they are split into two components separated by approximately 2000 cm^{-1} due to the spin-orbit splitting of the $4f^1$ ground state into two components $^2F_{5/2}$ and $^2F_{7/2}$. The bands observed in $Y_2O_2S:Ce^{3+}$ and $La_2O_2S:Ce^{3+}$ exhibit splitting by 5000 cm^{-1} and cannot be due to splitting of the ground stated mentioned above. Therefore, two

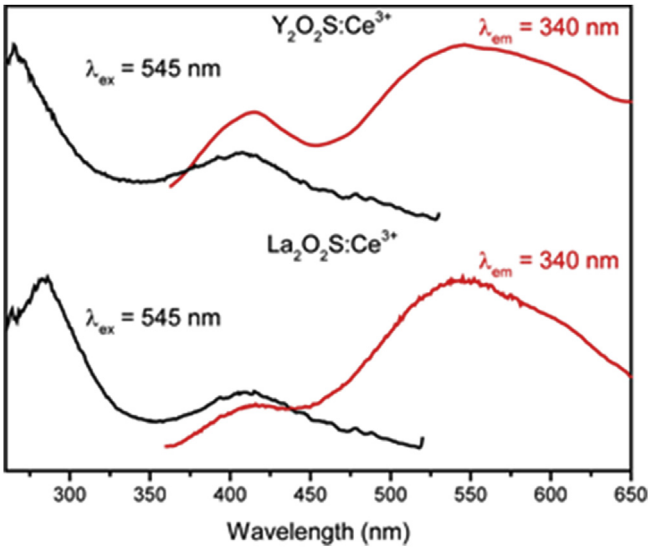

Fig. 7. Excitation and emission spectra of $Y_2O_2S:Ce^{3+}$ and $La_2O_2S:Ce^{3+}$phosphors.

bands ib Ce^{3+} luminescence must be ascribed to the electron transitions from the lowest and second 5d levels to the ground state of Ce^{3+}[53]. Change of host to La_2O_2S does not affect spectroscopic properties of Ce^{3+}-doped material. The line positions are almost the same for both excitation and emission spectra.

4. Conclusions

In summary, a method for the production of luminescent materials on the basis of rare-earth oxysulfides was developed. The advantage of the method consists in the precipitation of a sulfur-containing precursor from a homogeneous nitrate solution and subsequent transformation in a reducing and sulfidating atmosphere. The use of chemical homogenization made it possible to achieve an excellent uniform distribution of cations in the structure. The use of sulfates as precursors, in view of the presence of sulfur in the structure, greatly simplifies the process of obtaining solid solutions of oxysulfides. All synthesized samples have single phase without any impurities. The excitation and emission spectra of RE_2O_2S:Ln (RE = Y, La; Ln = Dy, Er, Eu) consist of characteristic bands corresponding to the 4f-4f intra configurational transitions. The study of Dy^{3+} and Eu^{3+}-doped powders revealed that Y_2O_2S host possesses higher local symmetry than La_2O_2S one. The excitation and emission spectra of $RE_2O_2S:Ce^{3+}$ (RE = Y, La) phosphor displayed allowed 5d–4f transition.

Acknowledgement

The authors would like to thank the staff of the Engineering Center of the Tyumen State University for their help in carrying out physical and chemical tests. We also thank Andrey Bobylev for conducting electron microscopy.

Appendix A. Supplementary data

Supplementary data to this article can be found online at https://doi.org/10.1016/j.jssc.2019.120964.

References

[1] YuG. Denisenko, A.S. Aleksandrovsky, V.V. Atuchin, A.S. Krylov, M.S. Molokeev, A.S. Oreshonkov, N.P. Shestakov, O.V. Andreev, Exploration of structural, thermal and spectroscopic properties of self-activated sulfate $Eu_2(SO4)_3$ with isolated SO_4 groups, J. Ind. Eng. Chem. 68 (2018) 109–116. https://doi.org/10.1016/j.jiec.2018.07.034.

[2] Y.G. Denisenko, V.V. Atuchin, M.S. Molokeev, A.S. Aleksandrovsky, A.S. Krylov, A.S. Oreshonkov, S.S. Volkova, O.V. Andreev, Structure, thermal stability, and spectroscopic properties of triclinic double sulfate $AgEu(SO_4)_2$ with Isolated SO_4 Groups, Inorg. Chem. 57 (21) (2018) 13279–13288. https://doi.org/10.1021/acs.inorgchem.8b01837.

[3] X. Shi, Z. Wang, T. Takei, X. Wang, Q. Zhu, X. Li, B.-N. Kim, X. Sun, J.-G. Li, Selective crystallization of four tungstates ($La_2W_3O_{12}$, $La_2W_2O_9$, $La_{14}W_8O_{45}$, and $La_6W_2O_{15}$) via hydrothermal reaction and comparative study of Eu^{3+} luminescence, Inorg. Chem. 57 (11) (2018) 6632–6640. https://doi.org/10.1021/acs.inorgchem.8b00807.

[4] F. Baur, T. Jüstel, Uranyl sensitized Eu^{3+} luminescence in $Ln(UO_2)_3(PO_4)_2$ $O(OH)\cdot 6H_2O$ phosphors (Ln = Y, Eu, La) for warm-white light emitting diodes, J. Lumin. 196 (2018) 431–436. https://doi.org/10.1016/j.jlumin.2017.12.073.

[5] V.V. Atuchin, A.S. Aleksandrovsky, O.D. Chimitova, T.A. Gavrilova, A.S. Krylov, M.S. Molokeev, A.S. Oreshonkov, B.G. Bazarov, J.G. Bazarova, Synthesis and spectroscopic properties of monoclinic α-$Eu_2(MoO_4)_3$, J. Phys. Chem. C 118 (28) (2014) 15404–15411. https://org/doi/10.1021/jp5040739.

[6] V.V. Atuchin, A.K. Subanakov, A.S. Aleksandrovsky, B.G. Bazarov, J.G. Bazarova, T.A. Gavrilova, A.S. Krulov, M.S. Molokeev, A.S. Oreshonkov, S.Yu Stefanovich, Structural and spectroscopic properties of noncentrosymmetric self-activated borate $Rb_3EuB_6O_{12}$ with B_5O_{10} units, Mater. Des. 140 (2018) 488–494. https://doi.org/10.1016/j.matdes.2017.12.004.

[7] J. Lian, F. Liu, J. Zhang, Y. Yang, X. Wang, Z. Zhang, F. Liu, Template-free hydrothermal synthesis of $Gd_2O_2SO_4:Eu^{3+}$ hollow spheres based on urea-ammonium sulfate (UAS) system, Optik 127 (20) (2016) 8621–8628. https://doi.org/10.1016/j.ijleo.2016.06.069.

[8] J. Lian, F. Liu, X. Wang, X. Sun, Hydrothermal synthesis and photoluminescence properties of $Gd_2O_2SO_4:Eu^{3+}$ spherical phosphor, Powder Technol. 253 (2014) 187–192. https://doi.org/10.1016/j.powtec.2013.11.021.

[9] X. Li, J. Lian, Synthesis and characterizations of pompon-like $Y_2O_2SO_4:Eu^{3+}$ phosphors using a UBHP technique based on UAS system, Optik 127 (1) (2016) 401–406. https://doi.org/10.1016/j.ijleo.2015.10.091.

[10] J. Lian, H. Qin, P. Liang, F. Liu, Co-precipitation synthesis of $Y_2O_2SO_4:Eu^{3+}$ nanophosphor and comparison of photoluminescence properties with Y_2O_3: Eu^{3+} and Y_2O_2S: Eu^{3+} nanophosphors, Solid State Sci. 48 (2015) 147–154. https://doi.org/10.1016/j.solidstatesciences.2015.08.004.

[11] H. Jiao, Y. Wang, $Ca_2Al_2Si_2O_7:Ce^{3+}$, Tb^{3+}: a white-light phosphor suitable for white light-emitting diodes, J. Electrochem. Soc. 156 (2009) J117–J120. http://jes.ecsdl.org/content/156/5/J117.short.

[12] R. Shrivastava, J. Kaur, V. Dubey, White light emission by Dy^{3+} doped phosphor matrices: a short review, J. Fluoresc. 26 (1) (2016) 105–111. https://doi.org/10.1007/s1089.

[13] F. Yang, H. Ma, Y. Liu, B. Han, H. Feng, Q. Yu, Photoluminescence properties of novel Dy^{3+} doped $Ba_5GaAl_4O_{12}$ phosphors, Ceram. Int. 40 (2014) 10189–10192. https://doi.org/10.1016/j.ceramint.2014.02.068.

[14] B.M. Cheng, C.K. Duan, P.A. Tanner, Vacuum ultraviolet and visible spectra of Eu^{3+} in Y_2O_2S and Eu_2O_2S, Opt. Mater. 31 (6) (2009) 902–904. https://doi.org/10.1016/j.optmat.2008.10.036.

[15] J. Thirumalai, R. Chandramohan, S. Valanarasu, T.A. Vijayan, R.M. Somasundaram, T. Mahalingam, S.R. Srikumar, Shape-selective synthesis and opto-electronic properties of Eu^{3+}- doped gadolinium oxysulfide nanostructures, J. Mater. Sci. 44 (14) (2009) 3889–3899. https://doi.org/10.1007/s10853-009-3531-7.

[16] X. Lu, L. Yang, Q. Ma, J. Tian, X. Dong, A novel strategy to synthesize $Gd_2O_2S:Eu^{3+}$ luminescent nanobelts via inheriting the morphology of precursor, J. Mater. Sci. Mater. Electron. 25 (12) (2014) 5388–5394. https://doi.org/10.1007/s10854-014-2317-0.

[17] S.A. Osseni, S. Lechevallier, M. Verelst, C. Dujardin, J. Dexpert-Ghys, D. Neumeyer, M. Leclercq, H. Baaziz, D. Cussac, V. Santran, R. Mauricot, New nanoplatform based on $Gd_2O_2S:Eu^{3+}$ core: synthesis, characterization and use for in vitro bio-labelling, J. Mater. Chem. 21 (45) (2011) 18365–18372. https://doi.org/10.1039/C1JM13542B.

[18] S.A. Osseni, S. Lechevallier, M. Verelst, P. Perriat, J. Dexpert-Ghys, D. Neumeyer, R. Garcia, F. Maye, K. Djanashvili, J.A. Peters, E. Magdeleine, H. Gros-Dagnac, P. Celsis, R. Mauricot, Gadolinium oxysulfide nanoparticles as multimodal imaging agents for T 2-weighted MR, X-ray tomography and photoluminescence, Nanoscale 6 (1) (2014) 555–564. https://doi.org/10.1039/C3NR03982J.

[19] Q. Zhao, Y. Zheng, N. Guo, Y. Jia, H. Qiao, W. Lv, H. You, 3D-hierarchical $Lu_2O_2S:Eu^{3+}$ micro/nano-structures: controlled synthesis and luminescence properties, CrystEngComm 14 (20) (2012) 6659–6664. https://doi.org/10.1039/C2CE25631B.

[20] Y. Yang, C. Mi, F. Yu, X. Su, C. Guo, G. Li, J. Zhang, L. Liu, Y. Liu, X. Li, Optical thermometry based on the upconversion fluorescence from Yb^{3+}/Er^{3+} codoped La_2O_2S phosphor, Ceram. Int. 40 (7 Part A) (2014) 9875–9880. https://doi.org/10.1016/j.ceramint.2014.02.081.

[21] S. Yokono, T. Abe, T. Hoshina, Red luminescence of Ce^{3+} to the large Stokes shifts in Y_2O_2S and Lu_2O_2S, J. Lumin. 24/25 (Part 1) (1981) 309–312. https://doi.org/10.1016/0022-2313(81)90279-9.

[22] Y. Yang, C. Mi, F. Yu, X. Su, C. Guo, G. Li, J. Zhang, L. Liu, Y. Liu, X. Li, Optical thermometry based on the upconversion fluorescence from Yb^{3+}/Er^{3+}codoped La_2O_2S phosphor//, Ceram. Int. 40 (2014) 9875–9880. № 7, Part A, https://doi.org/10.1016/j.ceramint.2014.02.081.

[23] X. Wang, Z. Zhang, Z. Tang, Y. Lin, Characterization and properties of a red and orange Y_2O_2S-based long afterglow phosphor, Mater. Chem. Phys. 80 (2003) 1–5. https://doi.org/10.1016/S0254-0584(02)00097-4.

[24] G.A. Kumar, M. Pokhrel, A. Martinez, R.C. Dennis, I.L. Villegas, D.K. Sardar, Synthesis and spectroscopy of color tunable $Y_2O_2S:Yb^{3+}$, Er^{3+} phosphors with intense emission, J. Alloy. Comp. 513 (2012) 559–565. https://doi.org/10.1016/j.jallcom.2011.11.006.

[25] T.W. Chou, S. Mylswamy, R.S. Liu, S.Z. Chuang, Eu substitution and particle size control of Y_2O_2S for the excitation by UV light emitting diodes, Solid State Commun. 136 (2005) 205–209. https://doi.org/10.1016/j.ssc.2005.07.032.

[26] H. Wang, M. Xing, X. Luo, X. Zhou, Y. Fu, T. Jiang, Y. Peng, Y. Ma, X. Duan, Up-conversion emission colour modulation of Y_2O_2S:Yb, Er under 1.55 μm and 980 nm excitation, J. Alloy. Comp. 587 (2014) 344–348. https://doi.org/10.1016/j.jallcom.2013.10.163.

[27] YuG. Denisenko, N.A. Khritokhin, O.V. Andreev, S.A. Basova, E.I. Sal'nikova, A.A. Polkovnikov, Thermal decomposition of europium sulfates $Eu_2(SO4)_3\cdot 8H_2O$ and $EuSO_4$, J. Solid State Chem. 255 (2017) 219–224. https://doi.org/10.1016/j.jssc.2017.08.020.

[28] H. Stark, R.L.N. Yatavelli, S.L. Thompson, H. Kang, J.E. Krechmer, J.R. Kimmel, B.B. Palm, W. Hu, P.L. Hayes, D.A. Day, P. Campuzano-Jost, M.R. Canagaratna, J.T. Jayne, D.R. Worsnop, J.L. Jimenez, Impact of thermal decomposition on thermal desorption instruments: advantage of thermogram analysis for quantifying volatility distributions of organic species, Environ. Sci. Technol. 51 (15) (2017) 8491–8500. https://doi.org/10.1021/acs.est.7b00160.

[29] O.V. Andrrev, I.A. Razumkova, A.N. Boiko, Synthesis and thermal stability of rare earth compounds REF_3, $REF_3\cdot nH2O$ and $(H_3O)RE_3F_{10}\cdot nH_2O$ (RE= Tb– Lu, Y), obtained from sulphide precursors, J. Fluorine Chem. 207 (2018) 77–83. https://doi.org/10.1016/j.jfluchem.2017.12.001.

[30] I.A. Razumkova, Synthesis of NaYF4 compounds from sulfide precursors, J. Fluorine Chem. 205 (2018) 1–4. https://doi.org/10.1016/j.jfluchem.2017.10.012.

[31] M. Unni, A.M. Uhl, S. Savliwala, B.H. Savitzky, R. Dhavalikar, N. Garraud, D.P. Arnold, L.F. Kourkoutis, J.S. Andrew, C. Rinaldi, Thermal decomposition synthesis of iron oxide nanoparticles with diminished magnetic dead layer by

controlled addition of oxygen, ACS Nano 11 (2) (2017) 2284–2303. https://doi.org/10.1021/acsnano.7b00609.
[32] S.A. Osseni, YuG. Denisenko, J.K. Fatombi, E.I. Sal'nikova, O.V. Andreev, Synthesis and characterization of $Ln_2O_2SO_4$ (Ln= Gd, Ho, Dy and Lu) nanoparticles obtained by coprecipitation method and study of their reduction reaction under H_2 flow, J. Nanostr. Chem. 7 (4) (2017) 337–343. https://doi.org/10.1007/s40097-017-0243-4.
[33] P.O. Andreev, E.I. Sal'nikova, O.V. Andreev, YuG. Denisenko, I.M. Kovenskii, Synthesis and upconversion luminescence spectra of $(Y_{1-x-y}Yb_xEr_y)_2O_2S$, Inorg. Mater. 53 (2) (2017) 200–206. https://doi.org/10.1134/S0020168517020029.
[34] P.O. Andreev, E.I. Sal'nikova, I.M. Kovenski, Preparation of Ln_2O_2S (Ln = Gd, Dy, Y, Er, Lu) in flowing hydrogen and hydrogen sulfide, Inorg. Mater. 50 (2014) 1018–1023. https://doi.org/10.1134/S0020168517020029.
[35] O.V. Andreev, YuG. Denisenko, E.I. Sal'nikova, N.A. Khritokhin, K.S. Zyryanova, Specifics of reactions of cerium sulfate and europium sulfate with hydrogen, Russ. J. Inorg. Chem. 61 (2016) 296–301. https://doi.org/10.1134/S0036023616030025.
[36] P.O. Andreev, E.I. Sal'nikova, O.V. Andreev, I.M. Kovenskii, Kinetic schemes of chemical transformations and particle morphology upon interaction between $Ln_2(SO_4)_3$ (Ln = La, Pr, Nd, Sm) and hydrogen//Russ, J. Phys. Chem. A 90 (1) (2016) 25–30. https://doi.org/10.1134/S0036024416010027.
[37] E.I. Sal´nikova, P.O. Andreev, S.M. Antonov, Kinetic diagrams of $Ln_2O_2SO_4$ phase transformations in a H_2 flow (Ln = La, Pr, Nd, Sm), Russ. J. Phys. Chem. A. 87 (8) (2013) 1280–1283. https://doi.org/10.1134/S0036024413080207.
[38] P.O. Andreev, E.I. Sal'nikova, A.A. Kislitsyn, Kinetics of the transformation of $Ln_2O_2SO_4$ into Ln_2O_2S (Ln = La, Pr, Nd, Sm) in a hydrogen flow, Russ. J. Phys. Chem. A. 87 (9) (2013) 1482–1487. https://doi.org/10.1134/S0036024413080050.
[39] Bruker AXS TOPAS V4, General Profile and Structure Analysis Software for Powder Diffraction Data. User's Manual, Bruker AXS, Karlsruhe, Germany, 2008.
[40] J. Kuang, Y. Liu, J. Zhang, White-light-emitting long-lasting phosphorescence in Dy^{3+}-doped SrSiO3, J. Solid State Chem. 179 (2006) 266–269. https://doi.org/10.1016/j.jssc.2005.10.025.
[41] P. Babu, K.H. Jang, E.S. Kim, L. Shi, H.J. Seo, F. Rivera-López, U.R. Rodriguez-Mendoza, V. Lavin, R. Vijaya, C.K. Jayasankar, L.R. Moorthy, Spectral investigations on Dy^{3+}-doped transparent oxyfluoride glasses and nanocrystalline glass ceramics, J. Appl. Phys. 105 (2009), 13516. https://doi.org/10.1063/1.3021451.
[42] I.E. Kolesnikov, A.A. Kalinichev, M.A. Kurochkin, E.V. Golyeva, A.S. Terentyeva, E.Yu Kolesnikov, E. Lähderanta, Structural, luminescence and thermometric properties of nanocrystalline YVO_4: Dy^{3+} temperature and concentration series, Sci. Rep. 9 (1) (2019) 2043. https://doi.org/10.1038/s41598-019-38774-6.
[43] I.E. Kolesnikov, A.V. Povolotskiy, D.V. Mamonova, E.Y. Kolesnikov, A.V. Kurochkin, E. Lähderanta, M.D. Mikhailov, Asymmetry ratio as a parameter of Eu^{3+} local environment in phosphors, J. Rare Earths 36 (2018) 474–481. https://doi.org/10.1016/j.jre.2017.11.008.
[44] E. Oomen, A.-M.A. Van Dongen, Europium (III) in oxide glasses: dependence of the emission spectrum upon glass composition, J. Non-Cryst. Solids 111 (1989) 205–213. https://doi.org/10.1016/0022-3093(89)90282-2.
[45] U. Fawad, H.J. Kim, S. Khan, M. Khan, L. Ali, Photoluminescent properties of white-light-emitting $Li_6Y(BO_3)_3$:Dy^{3+}phosphor, Solid State Sci. 62 (2016) 1–5. https://doi.org/10.1016/j.solidstatesciences.2016.08.008.
[46] Y.A. Dolinskaya, I.E. Kolesnikov, A.V. Kurochkin, A.A. Man'shina, M.D. Mikhailov, A.V. Semencha, Sol-gel synthesis and luminescent properties of YVO_4:Eu nanoparticles, Glass Phys. Chem. 39 (3) (2013) 308–310. https://doi.org/10.1134/S1087659613030061.
[47] I.E. Kolesnikov, A.V. Povolotskiy, D.V. Tolstikova, A.A. Manshina, M.D. Mikhailov, Luminescence of $Y_3Al_5O_{12}$: Eu^{3+} nanophosphors in blood and organic media, J. Phys. D Appl. Phys. 48 (7) (2015), 075401. https://doi.org/10.1088/0022-3727/48/7/075401/meta.
[48] I.E. Kolesnikov, D.V. Mamonova, E. Lähderanta, A.V. Kurochkin, M.D. Mikhailov, The impact of doping concentration on structure and photoluminescence of Lu_2O_3: Eu^{3+} nanocrystals, J. Lumin. 187 (2017) 26–32. https://doi.org/10.1016/j.jlumin.2017.03.006.
[49] Q. Dai, H. Song, M. Wang, X. Bai, B. Dong, R. Qin, X. Qu, H. Zhang, Size and concentration effects on the photoluminescence of La_2O_2S:Eu^{3+} nanocrystals, J. Phys. Chem. C 112 (49) (2008) 19399–19404. https://doi.org/10.1021/jp808343f.
[50] R.H. Krauss, R.G. Hellier, J.C. McDaniel, Surface temperature imaging below 300 K using La_2O_2S:Eu, Appl. Opt. 33 (18) (1994) 3901–3904. https://doi.org/10.1364/AO.33.003901.
[51] M. Upasani, B. Butey, S.V. Moharil, Synthesis, characterization and optical properties of $Y_3Al_5O_{12}$:Ce phosphor by mixed fuel combustion synthesis, J. Alloy. Comp. 650 (2015) 858–862. https://doi.org/10.1016/j.jallcom.2015.08.076.
[52] H.-L. Li, X.-J. Liu, L.-P. Huang, Luminescent properties of LuAG:Ce phosphors with different Ce contents prepared by a sol-gel combustion method, Opt. Mater. 29 (2007) 1138–1142. https://doi.org/10.1016/j.optmat.2006.05.002.
[53] J.-J. Zhao, C.-X. Guo, R.-W. Guo, J.-T. Hu, Red luminescence of Lu_2O_2S:Ce and Y_2O_2S:Ce at room temperature, J. Alloy. Comp. 436 (2007) 174–177. https://doi.org/10.1016/j.jallcom.2006.06.103.